J. Chem. Sci. (2019) 131:109
https://doi.org/10.1007/s12039-019-1686-6

REGULAR ARTICLE

Structure-dependence of electrical conductivity and electrocatalytic properties of $Sr_2Mn_2O_6$ and $CaSrMn_2O_6$

RAM KRISHNA HONA and FARSHID RAMEZANIPOUR*
Department of Chemistry, University of Louisville, Louisville, KY 40292, USA
E-mail: farshid.ramezanipour@louisville.edu

MS received 8 April 2019; revised 5 July 2019; accepted 23 July 2019; published online 7 November 2019

Abstract. Remarkable enhancement of the electrical conductivity and electrocatalytic activity is demonstrated as a result of the transformation of crystal structure between $Sr_2Mn_2O_6$ and $CaSrMn_2O_6$. The structure of $Sr_2Mn_2O_6$ is known to consist of dimeric units of face-sharing MnO_6 octahedra. Whereas, $CaSrMn_2O_6$ contains individual octahedra, connected to each other through corner-sharing. Herein we show that the changes in the crystal structure result in significant improvement of the electrical conductivity, by five orders of magnitude, for $CaSrMn_2O_6$, compared to $Sr_2Mn_2O_6$. Variable temperature conductivity studies from 25–800 °C indicate semiconducting properties for both compounds, where the enhanced conductivity of $CaSrMn_2O_6$ persists in the entire temperature range. The electrocatalytic activity of both compounds toward oxygen evolution reaction (OER) has also been investigated, indicating superior OER activity of $CaSrMn_2O_6$ compared to $Sr_2Mn_2O_6$. A pronounced improvement in the onset potential and kinetics of OER is observed for $CaSrMn_2O_6$. These studies demonstrate an important correlation between crystal structure, electrical conductivity and electrocatalytic properties.

Keywords. electrical conductivity; electrocatalysis; crystal structure.

1. Introduction

Perovskite oxides exhibit a wide range of structural, electrical and magnetic properties.[1–4] They have been studied for their potential applications in different technological fields, such as fuel cells, thermoelectric devices and sensors.[2,5,6] The structure and properties of perovskites can vary significantly[7–14] upon variation of the A- or B-site cations in the ABO_3 formula, where the A-cations occupy the 12-coordinated sites located between the BO_6 octahedra.

Given the wide range of transition metal or main group cations that can reside in the B-site, the structural transformation upon B-site doping are frequently observed. Various parameters, such as ionic radius, oxidation state and electronic structure lead to these changes. For example, when Mn is substituted by Fe, the orthorhombic structure of $CaMnO_3$[15] transforms into the orthorhombic structure of a double perovskite, Ca_2FeMnO_6, with layered ordering.[16,17] Similarly, Sr_2FeMoO_6 has a tetragonal structure, while the B-site substituted Sr_2FeWO_6 is orthorhombic.[18] The structural transformation leads to significant variations in properties as well, where Sr_2FeMoO_6 behaves as a half metal and a ferromagnetic material, whereas Sr_2FeWO_6 shows insulating and antiferromagnetic properties.[18] Note that there are two B-site cations in these materials. In situations, where there are two crystallographically distinct positions for the A- or B-site cations, the general formula can be represented by $AA'B_2O_6$ and $A_2BB'O_6$, respectively.

There are also oxide materials where the general formula is similar to that of a typical perovskite, but the connectivity in their crystal lattice is different. An example is $SrMnO_3$, better described as $Sr_2Mn_2O_6$ since it has two crystallographically distinct positions for Sr and two for Mn.[4] Unlike typical perovskites that contain corner-sharing octahedra, this material has dimeric units of face-sharing MnO_6 octahedra.[4] This compound has been of interest in recent years, given the potential of the Mn-based oxides for applications in areas such as sensing,[5] spintronics[19] and solid oxide fuel cells.[6] Several substituted derivatives have been investigated, showing variations in structure and properties. For example, when 50% of Mn in $Sr_2Mn_2O_6$ is substituted by Fe, the crystal structure changes to a perovskite-type system with corner-

*For correspondence

sharing octahedra.[20] The structural transformation also leads to changes in magnetic properties, where the antiferromagnetic arrangement of Mn^{4+} magnetic moments[4] in $Sr_2Mn_2O_6$ transforms into ferromagnetic arrangement upon partial substitution of Mn by Fe.[20]

It is also possible to partially or completely replace the A-site cation in $Sr_2Mn_2O_6$. For example, the Ba substitution on the A-site results in orthorhombic and rhombohedral structures for 50% and 100% substitutions, respectively.[21] The structural transformation upon Ba-doping is followed by the change in electrical properties.[21] It is also possible to replace Sr^{2+} by a smaller cation, namely Ca^{2+}, to obtain $CaSrMn_2O_6$, which has a perovskite-type structure[22], unlike the parent Sr_2 compound. To our knowledge, the effect of doping a smaller A-site cation, i.e., Ca^{2+}, on charge transport properties of $Sr_2Mn_2O_6$ has not been investigated. In this paper, we report the remarkable structure-property relationships, where the structural changes prompted by the replacement of the A-site cation lead to significant enhancement of the electrical charge-transport and electrocatalytic activity. A dramatic increase in the electrical conductivity is observed over a wide range of temperature, due to Ca-doping. Furthermore, we have studied the electrocatalytic activity of both $Sr_2Mn_2O_6$ and $CaSrMn_2O_6$ for oxygen-evolution reaction, demonstrating the enhancement of catalytic properties in the latter compound.

2. Experimental

The materials $Sr_2Mn_2O_6$ and $CaSrMn_2O_6$ were synthesized in air by solid-state method. Stoichiometric amounts of the powders of the precursor compounds $CaCO_3$ (Alfa Aesar, 99.95%), Mn_2O_3 (Alfa Aesar, 99.998%) and $SrCO_3$ (Sigma Aldrich, 99.99%) were mixed together using an agate mortar and pestle and pressed into a pellet which was calcined in air at 1000 °C for 24 h in order to decompose the carbonates and start the reaction. The samples were then ground and sintered at 1200 °C for 24 h in the same environment to complete the reaction and form pure products. Both heat treatments were followed by slow cooling. The heating and cooling rates were 100 °C/h. The phase purity and structure of the polycrystalline samples were examined by powder X-ray diffraction at room temperature using Cu Kα1 radiation (λ = 1.54056 Å). The GSAS software[23] and EXPEGUI interface[24] were used for Rietveld refinements. The sample morphologies were studied using high-resolution field-emission scanning electron microscopy (SEM). The electrical properties were investigated by 4-point probe measurements. Electrical conductivity was measured at 100 °C intervals from 25 to 800 °C during both heating and cooling cycles. At each measurement point, the temperature was maintained constant until a plateau in conductivity was observed, before changing the temperature. The rate of heating and cooling for conductivity measurements was 3 °C/min. Oxygen contents of each material were determined by iodometric titration as explained elsewhere.[14,25,26]

Electrocatalytic performances of the materials were measured in a three-electrode electrochemical workstation using a rotating disc electrode at 1600 rpm. A glassy carbon electrode loaded with catalysts, a commercial platinum electrode and Ag/AgCl (in 3 M NaCl) were used as working, counter and reference electrodes, respectively. For working electrode preparation, 35 mg of the sample and 20 μL of nafion (5% w/w in water/1-propanol) were mixed in 7 mL of THF and sonicated for 5 min. The catalyst ink was loaded onto the glassy carbon electrode (diameter 5 mm, area 0.196 cm^2) by four subsequent coatings (each coating with 10 μL). OER was performed in 0.1 M KOH electrolyte which was deaerated by bubbling argon gas for at least 30 min before the measurement started. The cyclic voltammetry (CV) measurements were performed at a scan rate of 10 mV s^{-1} from 0 to 0.8 V vs Ag/AgCl. The potential versus reversible hydrogen electrode (RHE) was calculated according to Nernst equation:

$$E_{RHE} = E_{Ag/AgCl} + 0.059\ pH + E^0_{Ag/AgCl}$$

3. Results and Discussion

3.1 *Crystal structure*

The X-ray diffraction studies demonstrate the structural changes due to the variation of the A-site cation in these $A_2B_2O_6$ compounds (A_2 = Sr_2, CaSr; B= Mn). The crystal structure of $Sr_2Mn_2O_6$ can be indexed on a hexagonal cell with space group $P6_3/mmc$, consistent with previous reports.[4] Rietveld refinement profile and the refined structural parameters from powder X-ray diffraction data are shown in Figure 1 and Table 1, respectively. As seen in Figure 1, the structure of $Sr_2Mn_2O_6$ consists of dimeric units of face-sharing MnO_6 octahedra. Each dimer is connected to other dimers through corner-sharing, leading to a 3-dimensional network. As shown in Table 1, there are two crystallographically distinct Sr sites and two distinct

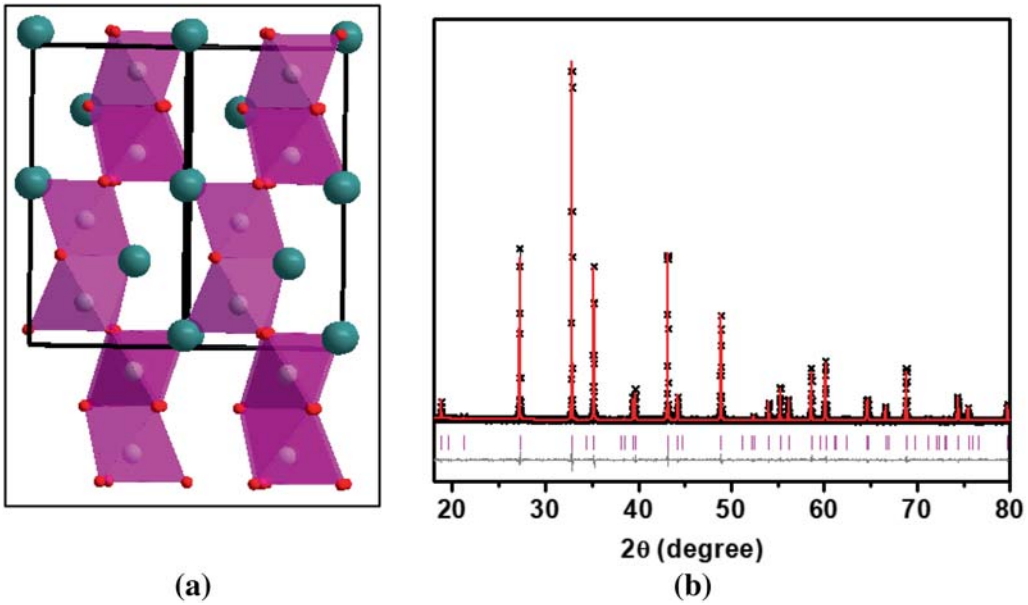

Figure 1. (a) Crystal structure and (b) Rietveld refinement profile from X-ray diffraction data for $Sr_2Mn_2O_6$, $P6_3/mmc$. Black crosses represent experimental data, the solid red line is the model, pink vertical tick marks show Bragg peak positions, and the lower grey line represents the difference plot.

Table 1. Refined structural parameters for $Sr_2Mn_2O_6$ using powder X-ray diffraction. Space group: $P6_3/mmc$, $a = b = 5.45233(8)$Å, c = 9.0856(1)Å, R_p= 0.030, wR_p = 0.038, χ^2 = 1.790.

Element	x	y	z	U_{iso}	Occupancy	Multiplicity
O1	0.191(8)	0.359(1)	0.298(2)	0.020(3)	1	6
O2	−0.021(3)	0.507(5)	0.049(2)	0.021(3)	1	6
Mn1	1/3	2/3	0.4160(8)	0.013(3)	1	2
Mn2	1/3	2/3	0.1412(8	0.046(4)	1	2
Sr1	1/3	2/3	0.7850(9)	0.0271(7)	1	2
Sr2	0.0	0.0	0.039(1)	0.0298(7)	1	2

Mn positions, hence the formula $Sr_2Mn_2O_6$. The crystal structure is transformed upon changing the A-site cations from Sr_2 to CaSr, as demonstrated in Figure 2. The Ca-containing compound, $CaSrMn_2O_6$, features a cubic $Pm\text{-}3m$ structure, where individual MnO_6 octahedra are all connected to each other through corner-sharing, consistent with a previous report.[22] There are no dimeric units in $CaSrMn_2O_6$, as shown in Figure 2. There is only one Mn position, and one A-site, jointly occupied by both Ca and Sr, as shown in Table 2 that lists the refined structural parameters for $CaSrMn_2O_6$.

We note that further substitution of Sr by Ca, beyond $CaSrMn_2O_6$, does not change the polyhedral connectivity. The completely substituted product, that contains only Ca on the A-site, contains the same type of corner-sharing connectivity as $CaSrMn_2O_6$, although the corner-sharing MnO_6 octahedra are somewhat distorted, leading to orthorhombic symmetry.[27] Nevertheless, the overall picture that emerges is that the transition from $Sr_2Mn_2O_6$ to $CaSrMn_2O_6$ results in significant structural transformation, but further substitution of Sr by Ca does not have a substantial effect on the structure type.

The Mn-O bond distances in $Sr_2Mn_2O_6$ vary widely, 1.81(2), 1.87(2), 1.91(2), and 2.03(2) Å, due to the existence of two types of polyhedral connectivity, namely face-sharing and corner-sharing. Given the structural differences between the two compounds, direct comparison of the bond distances is not warranted. However, the average Mn-O bond distance in $Sr_2Mn_2O_6$, 1.91 Å, is longer than that of $CaSrMn_2O_6$, 1.89 Å. Furthermore, the Mn-O-Mn bond angles in $Sr_2Mn_2O_6$ can be as small as 80.9(3)° due to the face-sharing in octahedral dimers. The angle between the corner-sharing octahedra in $Sr_2Mn_2O_6$ is Mn-O-

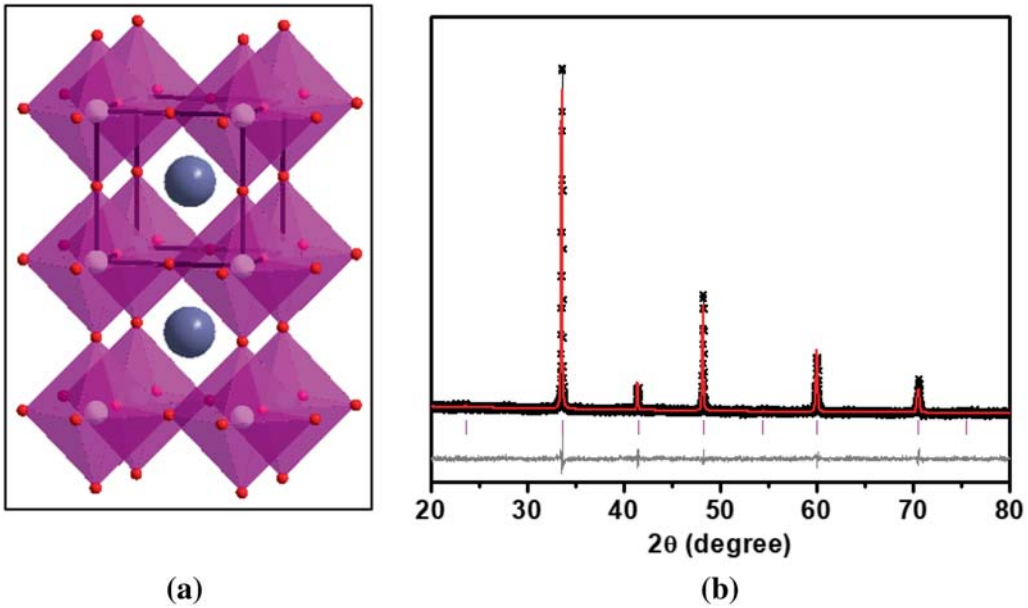

Figure 2. (a) Crystal structure and (b) Rietveld refinement profile from X-ray diffraction data for $CaSrMn_2O_6$, *Pm*-3*m*. Black crosses represent experimental data, the solid red line is the model, pink vertical tick marks show Bragg peak positions, and the lower grey line represents the difference plot.

Table 2. Refined structural parameters for $CaSrMn_2O_6$ using powder X-ray diffraction data. Space group: *Pm*-3*m*, a = 3.7772(1)Å, R_p = 0.051, wR_p = 0.064, χ^2 = 1.406.

	x	y	z	U_{iso}	Occupancy	Multiplicity
O1	0.5	0.0	0.0	0.043(2)	1	3
Mn1	0.0	0.0	0.0	0.007(1)	1	1
Ca1	0.5	0.5	0.5	0.024(2)	0.5	1
Sr1	0.5	0.5	0.5	0.024(2)	0.5	1

Mn = 166(1)°. However, $CaSrMn_2O_6$ contains only one type of Mn-O-Mn angle, which is 180°, as expected from a cubic perovskite structure.

3.2 *Electrical properties*

Changes in composition and the subsequent variation of the crystal structure lead to significant changes in the electrical properties, which were studied by four-probe technique. The electrical conductivity (σ) is obtained from the measured resistance (R), using the following equation:[28]

$$\sigma = L/RA \quad (1)$$

where L is the voltage probe spacing and A represents the cross-sectional area of the rectangular pellet where the current probes are connected. The remarkable effect of structural transformation is immediately clear from the improvement in the electrical conductivity by five orders of magnitude, 4.5×10^{-1} S cm^{-1} for $CaSrMn_2O_6$, compared to 1.0×10^{-6} S cm^{-1} for $Sr_2Mn_2O_6$ at room temperature. The electrical conductivity in oxide materials occurs through M–O–M pathways, where M is the transition metal. It has been demonstrated that larger bond angles lead to enhanced electrical conductivity due to the improved overlap between the metal 3d band and oxygen 2p band.[29] The change in crystal structure between $Sr_2Mn_2O_6$ and $CaSrMn_2O_6$ clearly leads to the enhancement of the Mn–O–Mn bond angles. The face sharing of MnO_6 octahedra in $Sr_2Mn_2O_6$ results in bond angles as small as 80.9(3)°, as described in the previous section. However, the Mn–O–Mn bond angles in $CaSrMn_2O_6$ are 180.0°, due to the cubic structure and corner-sharing between the octahedra.

The superior electrical conductivity of $CaSrMn_2O_6$ persists at a higher temperature, as evident from the results of conductivity studies in a wide temperature range, 25–800 °C, shown in Figure 3. Both compounds show an increase in conductivity as a function of temperature, a behavior typical of semiconductors. The increase in temperature results in the loss of oxygen and reduction of some of Mn^{4+} ions into Mn^{3+}, leading to facile charge transport through the resultant Mn^{4+}–O–Mn^{3+} pathways. In addition, the oxide ion conductivity is enhanced due to the creation of lattice defects upon oxygen loss. Furthermore, the rise in temperature leads to an increase in the mobility

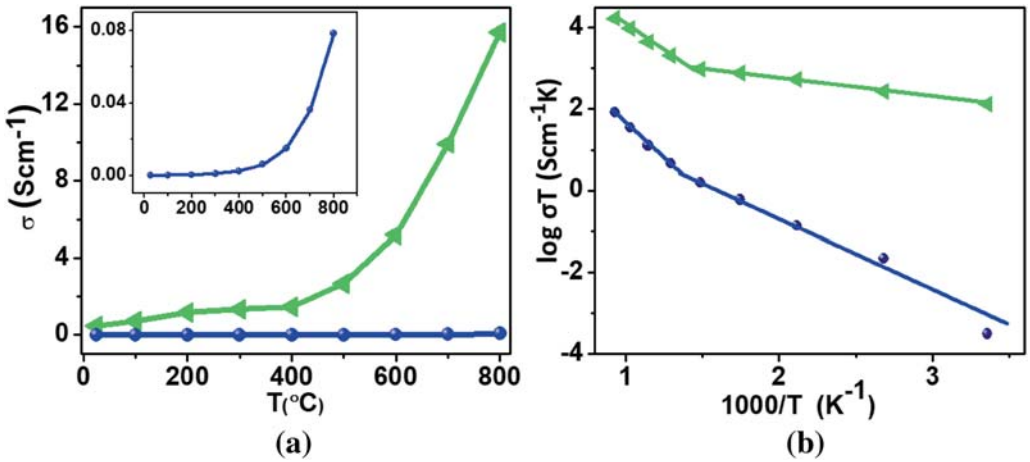

Figure 3. (a) Temperature-dependent electrical conductivity and (b) Arrhenius plots for $Sr_2Mn_2O_6$ (blue circles) and $CaSrMn_2O_6$ (green triangles). The inset in (a) is a zoomed view of the increase in conductivity of $Sr_2Mn_2O_6$.

of charge carriers, which in turn results in the enhancement of the electrical conductivity as described by the equation:

$$\sigma = ne\mu \quad (2)$$

where σ, n, e, and μ are the conductivity, concentration of charge carriers (electrons/holes), charge of the electron, and mobility of the charge carriers, respectively.

The activation energy for the increase in electrical conductivity as a function of temperature can be found using the Arrhenius equation for thermally activated conductivity:[30–32]

$$\sigma T = \sigma^0 e^{\frac{-E_a}{KT}} \quad (3)$$

where σ^0 is a pre-exponential factor and a characteristic of the material. Ea, K, and T are the activation energy for the increase in conductivity, Boltzmann constant, and absolute temperature, respectively. The activation energy (Ea) is calculated from the slope of the line of best fit in the log σT versus 1000/T plot (Figure 3). The Ea values for the sharp rise in conductivity above 500 °C are 0.687 eV for $Sr_2Mn_2O_6$ and 0.449 eV for $CaSrMn_2O_6$ (Table 3).

3.3 *Correlation between electrocatalytic activity and conductivity*

The electrocatalytic activity of these materials for oxygen evolution reaction (OER) was studied by cyclic voltammetry in alkaline medium. The OER mechanism in alkaline solution has been examined by several researchers.[50–52] The commonly accepted mechanism involves four steps, where there is a single electron transfer in each step.[50–52] In the first step, the reaction initiates by the adsorption of OH^- on the active site of the catalyst, i.e., metal site, M.[51,52] In the second step, a hydroxide from the electrolyte abstracts a proton from M-OH to form M-O and water. In the third step, M-O combines with a hydroxide to form a peroxide. Finally, in the fourth step, the peroxide intermediate reacts with OH^- to give an oxygen and water, and regenerate the catalyst.

1. $M + OH^- \rightarrow M\text{–}OH + e^-$
2. $M\text{–}OH + OH^- \rightarrow M\text{–}O + H_2O + e^-$
3. $M\text{–}O + OH^- \rightarrow M\text{–}OOH + e^-$
4. $M\text{–}OOH + OH^- \rightarrow M + H_2O + O_2 + e^-$

The conventional technique for investigation of OER activity involves the addition of carbon black to the electrode composition in order to enhance the electrical conductivity within the electrode and maximize the

Table 3. Room temperature conductivity and activation energies.

	Conductivity, σ (S cm^{-1})	Activation energy, E_a (eV)
$Sr_2Mn_2O_6$	1.0×10^{-6}	0.382 eV for 25 to 500 °C 0.687 eV for 500 to 800 °C
$CaSrMn_2O_6$	4.5×10^{-1}	0.093 eV for 25 to 400 °C 0.449 eV for 400 to 80 °C

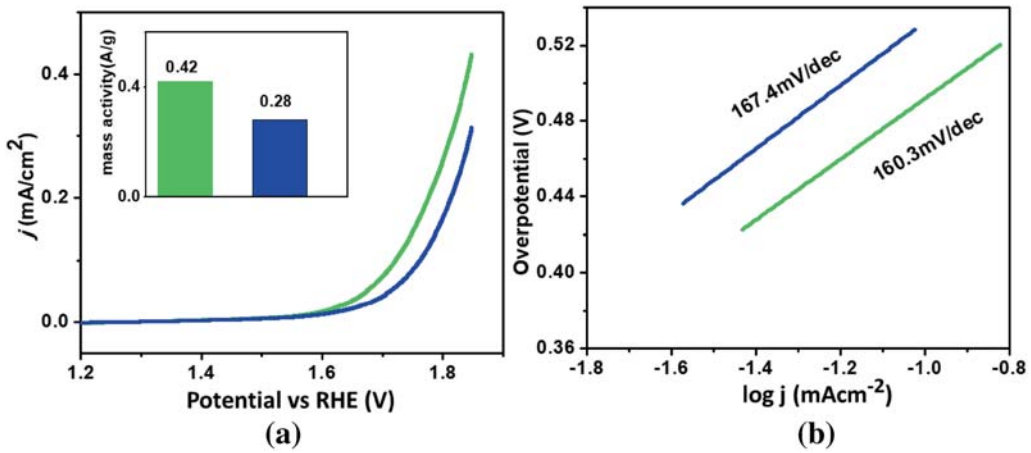

Figure 4. (a) Polarization curves for OER with mass activities for $Sr_2Mn_2O_6$ (blue) and $CaSrMn_2O_6$ (green). (b) Tafel slopes for $Sr_2Mn_2O_6$ (blue) and $CaSrMn_2O_6$ (green).

utilization of the catalyst.[33–35] However, recent studies have shown that the role of carbon is more complex than a simple enhancement of conductivity.[36,37] For example, it has been shown that cobalt in an OER catalyst is reduced by carbon during the composite preparation process.[38] Therefore, OER experiments without carbon black are prefered,[29] in order to examine the intrinsic catalytic activity of a material, without interference from carbon.[39] The two materials studied in this work demonstrate the effect of crystal structure and electrical conductivity on OER activity. As observed from Figure 4, $CaSrMn_2O_6$ shows significantly enhanced onset potential, $\sim$1.55 V, compared to $Sr_2Mn_2O_6$, $\sim$1.65 V. While these onset potentials are not as good as those of the state of the art catalysts materials, such as RuO_2, $\sim$1.45 V,[40] IrO_2, $\sim$1.50 V,[40] and BSCF, $\sim$1.53 V,[41] they are comparable to or better than those of several other reported catalysts, such as $CaMnO_3$/C (1.6 V),[40] Co-based microporous polymers, 1.57 V,[42] and Co-phthalocyanine, 1.70 V.[42] We have also determined the mass activity of each catalyst, using the catalyst loading mass on the electrode surface (0.2 mg cm^{-2}) and the measured current density for that electrode J (mA cm^{-2}). The inset in Figure 4 compares the OER mass activity of the two materials at 1.80 V vs RHE. As observed in this figure, $CaSrMn_2O_6$ shows mass activity of 0.42 A/g, compared to 0.28 A/g for $Sr_2Mn_2O_6$.

The kinetics of OER is usually examined using the Tafel equation $\eta = a + b \log j$ where η is the overpotential, and j is the current density.[44,45] The plot is obtained from the curved portion of the OER cyclic voltammogram, as commonly done in OER analysis.[48,49] The slope of the Tafel plot, η vs. log j, is used as a measure for the reaction kinetics and is influenced by electron and mass transportability of the catalyst.[46,47] The smaller slope is associated with faster reaction and indicates that once the reaction commences, it proceeds quickly without the need for significant increase in potential.[43] In other words, a small increase in potential leads to the generation of a significant current by OER process due to the fast kinetics of the reaction. A small change in the potential accompanied by a large increase in the current results in a small slope in the plot of η vs. log j. The Tafel slopes (Figure 4) for $CaSrMn_2O_6$ and $Sr_2Mn_2O_6$ are 160.3 mV/dec and 167.4 mV/dec, respectively, consistent with the greater OER activity of $CaSrMn_2O_6$ and the improved charge transport in this compound. These Tafel slopes are higher than those observed for highly active catalysts such as BSCF (87 mv/dec).[39] However, they are lower than the Tafel slopes for several other OER catalysts reported in the literature, with values ranging from 220 mV/dec,[53] to 184 mV/dec,[54] and 169 mV/dec.[55] The relationship between the electrical conductivity and OER activity is remarkable. $CaSrMn_2O_6$, which has superior electrical conductivity, also shows higher OER activity compared to $Sr_2Mn_2O_6$. These findings demonstrate an interesting correlation between crystal structure, electrical conductivity and electrocatalytic properties. The modification of the crystal structure can be used as a tool to enhance the electrical conductivity, which in turn can have an impact on the electrocatalytic properties.

4. Conclusions

The substitution of 50% of the A-site cations in $Sr_2Mn_2O_6$ results in the formation of $CaSrMn_2O_6$, which features a different crystal structure and polyhedral connectivity. The change in the crystal structure leads

to a significantly improved electrical conductivity in $CaSrMn_2O_6$. Variable-temperature electrical conductivity measurements indicate that the higher conductivity of $CaSrMn_2O_6$ persists up to 800 °C. The enhanced conductivity, in turn, results in the superior catalytic activity of $CaSrMn_2O_6$ for oxygen evolution reaction. These findings indicate the dependence of the electrical conductivity on the crystal structure, and the correlation between structure, charge-transport and electrocatalytic activity.

Acknowledgements

F. R. thanks the Conn Center for Renewable Energy Research. This work is supported in part by the National Science Foundation under Cooperative Agreement No. 1355438.

References

1. Lee K J and Iguchi E 1995 Electronic properties of $SrMnO_{3x}$ *J. Solid State Chem.* **114** 242
2. Kim C M, Seo J W, Choi S M, Seo W S, Lee S, Lim Y S and Park K 2015 Structural and thermoelectric properties of n-type $Sr_{1-x}Ti_xMnO_{3-\delta}$ perovskite system *Electron. Mater. Lett.* **11** 276
3. Suescun L, Chmaissem O, Mais J, Dabrowski B and Jorgensen J D 2007 Crystal structures, charge and oxygen-vacancy ordering in oxygen deficient perovskites $SrMnO_x$ ($x<2.7$) *J. Solid State Chem.* **180** 1698
4. Belik A, Matsushita Y, Katsuya Y, Tanaka M, Kolodiazhnyi T, Isobe M and Takayama-Muromachi E 2011 Crystal structure and magnetic properties of 6H-$SrMnO_3$ **84** 094438
5. Liu T, Yang, X, Ma C, Hao X, Liang X, Liu F, Liu F, Yang C, Zhu H and Lu G 2018 CeO_2-based mixed potential type acetone sensor using $MMnO_3$ (M: Sr, Ca, La and Sm) sensing electrode *Solid State Ionics* **317** 53
6. Ryu J, O'Hayre R and Lee H 2014 Structural analysis and electrochemical properties of cobalt-doped $Sr_{0.9}Ce_{0.1}MnO_{3-\delta}$ cathode for IT-SOFCs *J. Mater. Res.* **29** 2667
7. Anikina P V, Markov A A, Patrakeev M V, Leonidov I A and Kozhevnikov V L 2009 The structure, nonstoichiometry, and thermodynamic characteristics of oxygen in strontium ferrite doped with niobium, $SrFe_{1-x}Nb_xO_{3-\delta}$ *Russian J. Phys. Chem. A* **83** 699
8. 8. Zhu Z-L, Gu J-H, Jia Y and Hu X 2012 A comparative study of electronic structure and magnetic properties of $SrCrO_3$ and $SrMoO_3$ *Physic. B Cond. Matt.* **407** 1990
9. Zhang W, Meng J, Zhang X, Zhang L, Liu X and Meng J 2018 Co-incorporating enhancement on oxygen vacancy formation energy and electrochemical property of $Sr_2Co_{1+x}Mo_{1-x}O_{6-\delta}$ cathode for intermediate-temperature solid oxide fuel cell *Solid State Ionics* **316** 20
10. Gorodea I A 2014 Influence of the B-site cation nature on crystal structure and magnetic properties of Ca_2BMoO_6 (B = Cr, La, Sm) double perovskite *Acta Chemica Iasi* **22** 145
11. Hona R K, Huq A, Mulmi S and Ramezanipour F 2017 Transformation of structure, electrical conductivity, and magnetism in $AA'Fe_2O_{6-\delta}$, A = Sr, Ca and A′ = Sr *Inorg. Chem.* **56** 9716
12. Hona R K, Huq A and Ramezanipour F 2017 Unraveling the role of structural order in the transformation of electrical conductivity in $Ca_2FeCoO_{6-\delta}$, $CaSrFeCoO_{6-\delta}$, and $Sr_2FeCoO_{6-\delta}$ *Inorg. Chem.* **56** 14494
13. Mulmi S, Hona R K, Jasinski J B and Ramezanipour F 2018 Electrical conductivity of $Sr_{2-x}Ca_xFeMnO_5$ (x = 0, 1, 2) *J. Solid State Electrochem.* **22** 2329
14. Hona R K and Ramezanipour F 2018 Variation in electrical conductivity of $A_2Fe_2O_5$ (A = Sr, Ba): The role of structural order *Mater. Res. Express* **5** 076307
15. Molinari M, Tompsett D A, Parker S C, Azough F and Freer R 2014 Structural, electronic and thermoelectric behaviour of $CaMnO_3$ and $CaMnO_{(3-\delta)}$ *J. Mater. Chem. A* **2** 14109
16. Hosaka Y, Ichikawa N, Saito T, Manuel P, Khalyavin D, Attfield J P and Shimakawa Y 2015 Two-dimensional charge disproportionation of the unusual high valence state Fe^{4+} in a layered double perovskite *J. Am. Chem. Soc.* **137** 7468
17. Ganesanpotti S, Tassel C, Hayashi N, Goto Y, Bouilly G, Yajima T, Kobayashi Y and Kageyama H 2014 Charge disproportionation and magnetoresistivity in a double perovskite with Alternate Fe^{4+} (d^4) and Mn^{4+} (d^3) layers *Eur. J. Inorg. Chem.* **15** 2576
18. Chan T S, Liu R S, Hu S F and Lin J G 2005 Structure and physical properties of double perovskite compounds Sr_2FeMO_6 (M = Mo, W) *Mater. Chem. Phys.* **93** 314
19. Sayani M and Sebastiaan van D 2014 Pulsed laser deposition of $La_{1-x}Sr_xMnO_3$: thin-film properties and spintronic applications *J. Phys. D Appl. Phys.* **47** 034010
20. Cui L and Yang L 2012 Magnetic and transport properties of the double perovskite Sr_2FeMnO_6 *Adv. Mater. Res.* **393–395** 157
21. Markiewicz E, Bujakiewicz-Koronska R, Budziak A, Kalvane A and Nalecz D M 2014 Impedance spectroscopy studies of $SrMnO_3$, $BaMnO_3$ and $Ba_{0.5}Sr_{0.5}MnO_3$ ceramics *Phase Trans.* **87** 1060
22. Töpfer J, Pippardt U, Voigt I and Kriegel R 2004 Structure, nonstoichiometry and magnetic properties of the perovskites $Sr_{1-x}Ca_xMnO_{3-\delta}$ *Solid State Sci.* **6** 647
23. Larson A C and Von Dreele A C 1994 General structure analysis system (GSAS). *Los Alamos National Laboratory Report LAUR*, 86–748.
24. Toby B H 2001 EXPGUI, a graphical user interface for GSAS *J. Appl. Crystallogr.* **34** 210
25. Hona R K and Ramezanipour F 2018 Disparity in electrical and magnetic properties of isostructural oxygen-deficient perovskites $BaSrCo_2O_{6-\delta}$ and $BaSrCoFeO_{6-\delta}$ *J. Mater. Sci. Mater. Electron.* **29** 13464
26. Hona R K, Huq A and Ramezanipour F 2018 Electrical properties of the ordered oxygen-deficient perovskite $Ca_2Fe_{0.5}Ga_{1.5}O_5$ *Ionics* **25** 1315
27. Aschauer U, Pfenninger R, Selbach S M, Grande T and Spaldin N A 2013 Strain-controlled oxygen vacancy

formation and ordering in $CaMnO_3$ *Phys. Rev. B* **88** 054111
28. Singh Y 2013 Electrical resistivity measurements: A review *Int. J. Modern Phys. Conf. Series* **22** 745
29. Cheng X, Fabbri E, Nachtegaal M, Castelli I E, El Kazzi M, Haumont R, Marzari N and Schmidt T J 2015 Oxygen evolution reaction on $La_{1-x}Sr_xCoO_3$ perovskites: A combined experimental and theoretical study of their structural, electronic, and electrochemical properties *Chem. Mater.* **27** 7662
30. Pizzini S 2015 *Physical chemistry of semiconductor materials and processes* (West Sussex, United Kingdom: John Wiley)
31. Asenath-Smith E, Lokuhewa I N, Misture S T and Edwards D D 2010 p-Type thermoelectric properties of the oxygen-deficient perovskite $Ca_2Fe_2O_5$ in the brownmillerite structure *J. Solid State Chem.* **183** 1670
32. Andoulsi R, Horchani-Naifer K and Férid M 2013 Electrical conductivity of $La_{1-x}Ca_xFeO_{3-\delta}$ solid solutions *Ceram. Int.* **39** 6527
33. Jin C, Cao X, Zhang L, Zhang C and Yang R 2013 Preparation and electrochemical properties of urchin-like $La_{0.8}Sr_{0.2}MnO_3$ perovskite oxide as a bifunctional catalyst for oxygen reduction and oxygen evolution reaction *J. Power Sources* **241** 225
34. May K J, Carlton C E, Stoerzinger K A, Risch M, Suntivich J, Lee Y L, Grimaud A and Shao Horn Y 2012 Influence of oxygen evolution during water oxidation on the surface of perovskite oxide catalysts *J. Phys. Chem. Lett.* **3** 3264
35. Malkhandi S, Trinh P, Manohar A K, Jayachandrababu K C, Kindler A, Surya Prakash G K and Narayanan S R 2013 Electrocatalytic activity of transition metal oxide-carbon composites for oxygen reduction in alkaline batteries and fuel cells *J. Electrochem. Soc.* **160** 943
36. Liang Y, Li Y, Wang H, Zhou J, Wang J, Regier T and Dai H 2011 Co_3O_4 nanocrystals on graphene as a synergistic catalyst for oxygen reduction reaction *Nat. Mater.* **10** 780
37. Mohamed R, Cheng X, Fabbri E, Levecque P, Kötz R, Conrad O and Schmidt T J 2015 Electrocatalysis of perovskites: The influence of carbon on the oxygen evolution activity *J. Electrochem. Soc.* **162** 579
38. Fabbri E, Nachtegaal M, Cheng X and Schmidt Thomas J 2015 Superior bifunctional electrocatalytic activity of $Ba_{0.5}Sr_{0.5}Co_{0.8}Fe_{0.2}O_{3-\delta}$/carbon composite electrodes: Insight into the local electronic structure *Adv. Energy Mater.* **5** 1402033
39. Hona R K and Ramezanipour F 2019 Remarkable oxygen-evolution activity of a perovskite oxide from the $Ca_{2-x}Sr_xFe_2O_{6-\delta}$ Series *Angew. Chem. Int. Ed.* **58** 2060
40. Kim J, Yin X, Tsao K C, Fang S and Yang H 2014 $Ca_2Mn_2O_5$ as oxygen-deficient perovskite electrocatalyst for oxygen evolution reaction *J. Am. Chem. Soc.* **136** 14646
41. Zhu Y, Zhou W, Chen Z G, Chen Y, Su C, Tadé Moses O and Shao Z 2015 $SrNb_{0.1}Co_{0.7}Fe_{0.2}O_{3-\delta}$ perovskite as a next-generation electrocatalyst for oxygen evolution in alkaline solution *Angew. Chem. Int. Ed.* **54** 3897
42. Singh A, Roy S, Das C, Samanta D and Maji T K 2018 Metallophthalocyanine-based redox active metal–organic conjugated microporous polymers for OER catalysis *Chem. Commun.* **54** 4465
43. Shinagawa T, Garcia-Esparza A T and Takanabe K 2015 Insight on Tafel slopes from a microkinetic analysis of aqueous electrocatalysis for energy conversion *Sci. Rep.* **5** 13801
44. Pan Y, Chen Y, Li X, Liu Y and Liu C 2015 Nanostructured nickel sulfides: phase evolution, characterization and electrocatalytic properties for the hydrogen evolution reaction *RSC Adv.* **5** 104740
45. Oh S, Kim H, Kwon Y, Kim M, Cho E and Kwon H 2016 Porous Co–P foam as an efficient bifunctional electrocatalyst for hydrogen and oxygen evolution reactions *J. Mater. Chem. A* **4** 18272
46. Song F, Hu X 2014 Ultrathin cobalt–manganese layered double hydroxide Is an efficient oxygen evolution catalyst *J. Am. Chem. Soc.* **136** 16481
47. Moir J, Soheilnia N, O'Brien P, Jelle A, Grozea C M, Faulkner D, Helander M G and Ozin G A 2013 Enhanced hematite water electrolysis using a 3D antimony-doped tin oxide electrode *ACS Nano* **7** 4261
48. Zhang W, Zhang X, Chen L, Dai J, Ding Y, Ji L, Zhao J, Yan M, Yang F, Chang C-R and Guo S 2018 Single-walled carbon nanotube induced optimized electron polarization of rhodium nanocrystals to develop an interface catalyst for highly efficient electrocatalysis *ACS Catal.* **8** 8092
49. Zhu Y, Zhou W, Yu J, Chen Y, Liu M and Shao Z 2016 Enhancing electrocatalytic activity of perovskite oxides by tuning cation deficiency for oxygen reduction and evolution reactions *Chem. Mater.* **28** 1691
50. Zhu Y, Zhou W, Sunarso J, Zhong Y and Shao Z 2016 Phosphorus-doped perovskite oxide as highly efficient water oxidation electrocatalyst in alkaline solution *Adv. Funct. Mater.* **26** 5862
51. Rong X, Parolin J and Kolpak A M 2016 A fundamental relationship between reaction mechanism and stability in metal oxide catalysts for oxygen evolution *ACS Catal.* **6** 1153
52. Wang J, Gao Y, Chen D, Liu J, Zhang Z, Shao Z and Ciucci F 2018 Water splitting with an enhanced bifunctional double perovskite *ACS Catal.* **8** 364
53. Ranaweera C K, Zhang C, Bhoyate S, Kahol P K, Ghimire M, Mishra S R, Perez F, Gupta B K and Gupta R K 2017 Flower-shaped cobalt oxide nano-structures as an efficient, flexible and stable electrocatalyst for the oxygen evolution reaction *Mater. Chem. Front.* **1** 1580
54. Joya K S, Ul Ain Babar N, Gilani S R, Yasmeen F, Sarfaraz M, Ikram S, Colak S G, Ocakoglu K and Ince M 2018 Heterogeneous electrocatalysts for efficient water oxidation derived from metal phthalocyanine *Chem. Select* **3** 11357
55. Lv X, Zhu Y, Jiang H, Yang X, Liu Y, Su Y, Huang J, Yao Y and Li C 2015 Hollow mesoporous $NiCo_2O_4$ nanocages as efficient electrocatalysts for oxygen evolution reaction *Dalton Trans.* **44** 4148